



Pseudocapacitance enhanced by N-defects in $\text{Na}_3\text{MnTi}(\text{PO}_4)_3$ /N-doped carbon composite for symmetric full sodium-ion batteries



H. Li ^{a, b, c}, W. Zhang ^{b, c}, Z. Han ^b, K. Sun ^b, C. Gao ^b, K. Cheng ^a, Z. Liu ^a, Q. Chen ^a, J. Zhang ^a, Y. Lai ^b, Z. Zhang ^{b, *}, H. Sun ^{a, **}

^a Department of Chemistry, City University of Hong Kong, Kowloon, Hong Kong, China

^b School of Metallurgy and Environment, Central South University, Changsha 410083, PR China

ARTICLE INFO

Article history:

Received 15 March 2021

Received in revised form

5 April 2021

Accepted 8 April 2021

Available online 14 April 2021

Keywords:

NASICON

Symmetric full battery

$\text{Na}_3\text{MnTi}(\text{PO}_4)_3$

N-defects

Pseudocapacitance

ABSTRACT

The concept of symmetric full battery attracts increasing attention in recent years. The symmetric battery consists of two identical 'bifunctional' electrode materials, which can be used as both the cathode and anode. The NASICON-structured $\text{Na}_3\text{MnTi}(\text{PO}_4)_3$ is capable to be used as a bifunctional electrode for symmetric sodium-ion full battery because of its multiredox reaction with a suitable voltage gap. However, it suffers from limited capacity and poor rate performance. In this study, $\text{Na}_3\text{MnTi}(\text{PO}_4)_3$ particulates embedding in the N-doped carbon matrix material (NMTP/C–N) are constructed. Both the experiments and density functional theory (DFT) calculations show that the N-defects in the carbon matrix have stronger adsorption energy toward Na^+ , and the N-vacancy defects have lower diffusion barriers for sodium-ion diffusion, thus enabling higher pseudocapacitance of the NMTP/C–N. By virtue of the enhanced reaction kinetics and pseudocapacitance, the NMTP/C–N demonstrates improved specific capacity and high-rate capability in both high- and low-voltage ranges (2.5–4.2 V vs. Na/Na^+ ; 1.5–2.5 V vs. Na/Na^+), where it is operated as the cathode and anode basing on the redox of $\text{Mn}^{2+}/\text{Mn}^{4+}$ and $\text{Ti}^{4+}/\text{Ti}^{3+}$, respectively. When constructed to a symmetric full battery, it exhibits a moderate reversible capacity of 91.8 mAh/g with a high initial Columbic efficiency of 85.2%, and maintains 70.8% of discharge capacity after 400 cycles at 1C. This work deepens our understanding of materials design for enhanced pseudocapacitance and electrochemical performances.

© 2021 Elsevier Ltd. All rights reserved.

1. Introduction

To reduce the impact of fossil energy on environment and global climate, research on renewable energy sources has been growing vigorously in recent decades [1–4]. Rechargeable battery technologies are vital for large-scale renewable energy storage. Lithium-ion batteries (LIBs) are famous for their high energy density and long lifespan. However, the proliferation of LIBs in portable electronics and electric vehicles makes lithium resources too expensive to be applied to large-scale energy storage [5–9]. Sodium-ion batteries (SIBs) have been considered as a promising alternative because of the abundant sodium resources and low cost [10,11].

Besides, SIBs share identical principles and similar physicochemical properties with LIBs, so that the development of SIBs can follow the pathway of LIBs. To date, various cathodes, anodes, and electrolyte materials have been explored and exhibited good sodium storage performance, but fabrication of full cells with high energy density, long cycling life, and flexible rate capability is still a big challenge [11,12].

Among the effort to develop full cells for SIBs, recently, symmetric battery systems attract more and more attention [13–15]. Different from asymmetric battery, where the cathode is generally oxides or polyanion-type materials and the anode is carbon-based materials, symmetric battery consists of two identical 'bi-functional' electrode materials, which can be used as both the cathode and anode. It is suggested to insert/extract sodium-ions at different voltage range basing on the redox of different transition metal ions. Therefore, symmetric full cell has the following advantages: firstly, from a commercial perspective, it simplifies the configuration and fabrication of full cells, leading to lower manufacturing cost;

* Corresponding author.

** Corresponding author.

E-mail addresses: zhangzhian@csu.edu.cn (Z. Zhang), hongysun@cityu.edu.hk (H. Sun).

^c These authors contributed equally to this work.

secondly, volume expansion of the electrode materials and sodium dendrites can be mitigated, enabling better cycling stability and higher safety of the battery system. Nevertheless, few bifunctional electrode materials were developed. Despite the progress achieved by transition metal oxides [16–18], lately, the sodium superionic conductor (NASICON)-structured materials are particularly attractive because of their outstanding thermal stability and three-dimensional crystallographic structure with spacious ion diffusion pathways [19,20]. More importantly, the tunable transition metal ions in the NASICON structure provide numerous possibilities for designing bifunctional materials. The well-documented $\text{Na}_3\text{V}_2(\text{PO}_4)_3$ is a typical bifunctional material, which can be used as a cathode basing on the variation of $\text{V}^{4+}/\text{V}^{3+}$ at 3.4 V (vs. Na^+/Na), and as an anode basing on the redox of $\text{V}^{3+}/\text{V}^{2+}$ at 1.6 V [21]. Other NASICON-structured materials such as $\text{Na}_2\text{VTi}(\text{PO}_4)_3$ [22] and $\text{Na}_2\text{LiV}_2(\text{PO}_4)_3$ [23] were also investigated in symmetric battery systems. Recently, a new NASICON electrode material $\text{Na}_3\text{MnTi}(\text{PO}_4)_3$ was proposed by Goodenough's group [24,25]. The $\text{Na}_3\text{MnTi}(\text{PO}_4)_3$ can realize three-electron reaction by virtue of the redox of $\text{Mn}^{2+}/\text{Mn}^{3+}$, $\text{Mn}^{3+}/\text{Mn}^{4+}$, and $\text{Ti}^{3+}/\text{Ti}^{4+}$ at distinctive potentials of 3.6, 4.1, and 2.1 V, respectively. Besides, the $\text{Na}_3\text{MnTi}(\text{PO}_4)_3$ has demonstrated good rate capability and cycling stability in aqueous symmetric battery systems. However, in the aqueous systems, to avoid water decomposition, only $\text{Mn}^{2+}/\text{Mn}^{3+}$ and $\text{Ti}^{3+}/\text{Ti}^{4+}$ redox couples were activated in $\text{Na}_3\text{MnTi}(\text{PO}_4)_3$, thus it delivered a limited reversible capacity of 58.4 mAh/g with a platform at 1.4 V [24]. The energy density of this material is supposed to be further improved in non-aqueous symmetric systems. However, the electrochemical performance of $\text{Na}_3\text{MnTi}(\text{PO}_4)_3$ is hindered by limited capacity, poor electronic conductivity, and sluggish ion-exchange dynamics, which are imperative to be addressed for assembling symmetric full battery. Compositing with carbon materials such as CNTs, graphene, and amorphous carbon to construct advanced composite structures has been proven effective to mitigate these problems [26,27]. The introduction of carbon materials can not only increase electronic conductivity, but also, in particular, help to enhance the contribution of pseudocapacitance, leading to higher capacity and rate performances of the electrode. Note that, understanding the mechanism of the enhanced pseudocapacitance that derived from carbon materials is still rare.

Herein, to assemble an advanced symmetric full battery, we aim at increasing the reaction kinetics and pseudocapacitance of $\text{Na}_3\text{MnTi}(\text{PO}_4)_3$, and successfully synthesized $\text{Na}_3\text{MnTi}(\text{PO}_4)_3$ particulates embedding in the N-doped carbon matrix material (NMTP/C–N) through a facile sol–gel method. Various N active sites and N-vacancies were found beneficial to adsorb sodium-ions and lowering the energy barrier for sodium-ion passing through the carbon layer for a redox reaction, enabling enhanced pseudocapacitance effect. In addition, combining with the advanced composite structure with improved electronic conductivity, reduced particle size, and abundant reactive sites, electrochemical performance of the NMTP/C–N was greatly improved, showing good cycling stability with 88.1% and 93.2% of capacity retention after 350 cycles at 2C as the cathode and anode, respectively. Based on this, a stable non-aqueous symmetric full battery with a reversible capacity of 91.8 mAh/g was finally assembled.

2. Results and discussion

X-ray diffraction (XRD) patterns of both the NMTP/C–N and NMTP/C materials can be indexed to standard $\text{Na}_3\text{MnTi}(\text{PO}_4)_3$ with a rhombohedral NASICON structure (Fig. 1a), where interstitials that constructed by the corner-shared $[\text{Mn}/\text{TiO}_6]$ octahedra and $[\text{PO}_4]$ tetrahedra are occupied by the immobile Na1 and mobile Na2 [25]. The two samples show similar peak intensity, indicating

similar crystallinity of the materials. Rietveld refinement on the XRD pattern of NMTP/C–N material was performed to further check the phase of $\text{Na}_3\text{MnTi}(\text{PO}_4)_3$, and the fitting results with $R_p = 4.59\%$ and $R_{wp} = 6.38\%$ were acceptable (Fig. S1). The rhombohedral cell shows lattice parameters of $a = 8.816939$ Å, $c = 21.768875$ Å, and $V = 1,465.556$ Å³. No other phases were detected, indicating the high purity of the NMTP/C–N material. Morphology of the samples is investigated by scanning electron microscopy and transmission electron microscope (TEM). As demonstrated in Figs. 1b and S2a, both of the NMTP/C–N and NMTP/C composites are irregular in shapes, and TEM images (Figs. 1c and S2b) show that the NMTP particles are embedded in the carbon matrix. The carbon content was 14.52% and 12.09% for NMTP/C–N and NMTP/C, respectively, which were measured by organic elemental analysis. The high-resolution TEM in Fig. 1d further identified the microstructure of the NMTP/C–N composite. The NMTP particle that is confined in the carbon matrix shows lattice fringes with a d-spacing of about 0.377 nm, corresponding to the (202) plane of $\text{Na}_3\text{MnTi}(\text{PO}_4)_3$ material, which can be further confirmed by the fast Fourier transform images (Fig. 1e). The energy dispersive spectrometer (EDS) mapping profiles demonstrate homogeneous distribution of Na, Mn, Ti, P, O, C, and N elements in the NMTP/C–N (Fig. 1f).

X-ray photoemission spectroscopy (XPS) was used to analyze the elemental state and bonding structure of the materials. Binding energy of the Mn 2p peaks show that both Mn^{2+} (652.87 eV for Mn 2p_{1/2}, 641.11 eV for Mn 2p_{3/2}) and Mn^{3+} are existed in $\text{Na}_3\text{MnTi}(\text{PO}_4)_3$ (Fig. 2a) [28–31]. Similarly, Ti^{3+} (463.95 eV for Ti 2p_{1/2}, 458.42 eV for Ti 2p_{3/2}) and Ti^{4+} (465.56 eV for Ti 2p_{1/2}, 459.82 eV for Ti 2p_{3/2}) are also found co-existed (Fig. 2b) [30,31]. Based on the XPS results, fractions of Mn^{3+} and Ti^{3+} in the total amount of Mn and Ti were calculated to be 54.4% and 56.8%, respectively. N-species are detected in NMTP/C–N, but not in NMTP/C (Fig. S3). Nitrogen content in NMTP/C–N was measured to be 0.13% by organic elemental analysis. The N 1s spectra show peaks located at 403.01, 400.35, 399.58, and 398.25 eV can be assigned to oxidized N, graphitic N, pyrrolic N, and pyridinic N, respectively (Fig. 2c) [32]. The C 1s peaks that appeared at 288.63 and 285.34 eV are attributed to C–N and C=N bonds (Fig. 2d) [32,33]. These results confirm that N species are successfully introduced in the carbon matrix. The pyrrolic-N and pyridinic-N defects can damage the carbon structure and cause many exposed N/vacancy defects [32]. As a result, the NMTP/C–N demonstrates a larger specific surface area ($39.54 \text{ m}^2/\text{g}$) and pore volume ($0.073 \text{ cm}^3/\text{g}$) than those of the NMTP/C, which has a specific surface area of $11.97 \text{ m}^2/\text{g}$ and pore volume of $0.022 \text{ cm}^3/\text{g}$. The defects also lead to a more disordered carbon structure [34], which is confirmed by the larger I_D/I_G value of NMTP/C–N (1.02) than that of NMTP/C (0.98) (Fig. 2f). As the electronegativity of N is higher than that of C, the N-defects should be negatively charged. In that case, the positively charged Na^+ can be easily adsorbed in the defects due to the static forces. Besides, because of the porous structure and abundant vacancy defects, the Na^+ can facilely pass through the carbon larger for fast sodium-ion storage reaction [34]. The N-defects, interaction between N and Na^+ , and schematic of the fast electron/ion-exchange reaction in NMTP/C–N are illustrated in Fig. 2g–i, respectively.

Electrochemical performances of the materials as both positive and negative electrodes in half cells were investigated within the voltage window of 2.5–4.2 V and 1.5–2.5 V, respectively. According to Fig. 3a, as a cathode, the NMTP/C–N exhibits an initial specific capacity of 94.5 mAh/g at 0.05C (1C = 100 mA/g). The charge/discharge curves of the NMTP/C–N shows two flat voltage plateaus of 3.56/3.51 and 4.07/4.03 V, which was confirmed by the dQ/dV plots (inset in Fig. 3a), and they correspond to the redox of $\text{Mn}^{2+}/\text{Mn}^{3+}$ and $\text{Mn}^{3+}/\text{Mn}^{4+}$, respectively. Such high operating potentials

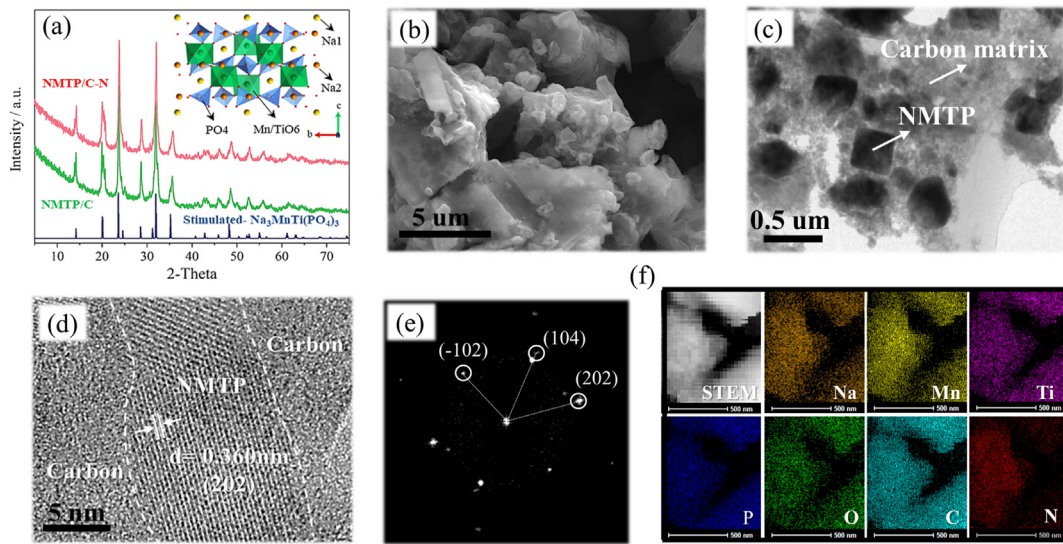


Fig. 1. Physical and chemical characterization of the NMTP/C–N and NMTP/C materials. (a) XRD patterns and the inset is the schematic illustration of the crystal structure of $\text{Na}_3\text{MnTi}(\text{PO}_4)_3$. (b) Scanning electron microscope, (c) TEM, and (d) high-resolution TEM images of the NMTP/C–N material. (e) The fast Fourier transform patterns of the NMTP/C–N. (f) Elemental mapping images of the NMTP/C–N.

and satisfactory capacity are beneficial for the fabrication of high energy density full cells. Comparison of rate performances of the different cathodes is shown in Fig. 3b. NMTP/C–N is able to deliver a reversible capacity of 94.5, 83.7, 74.5, 66.4, 60.4, 53.1, and 38.5 mAh/g at 0.05, 0.1, 0.2, 0.5, 1, 2, and 5C, respectively. When the current density turns back to 0.2C from 5C, the discharge capacity

of the material recovers to 73.2 mAh/g, indicating a highly flexible rate performance of the cathode. Notably, after 100 cycles at 0.2C, a reversible capacity of 68.2 mAh/g can be obtained, which corresponds to 93.2% of its initial capacity, indicating outstanding reversibility of the electrode. However, for the NMTP/C, it shows a lower discharge capacity than the NMTP/C–N, and the capacity gap

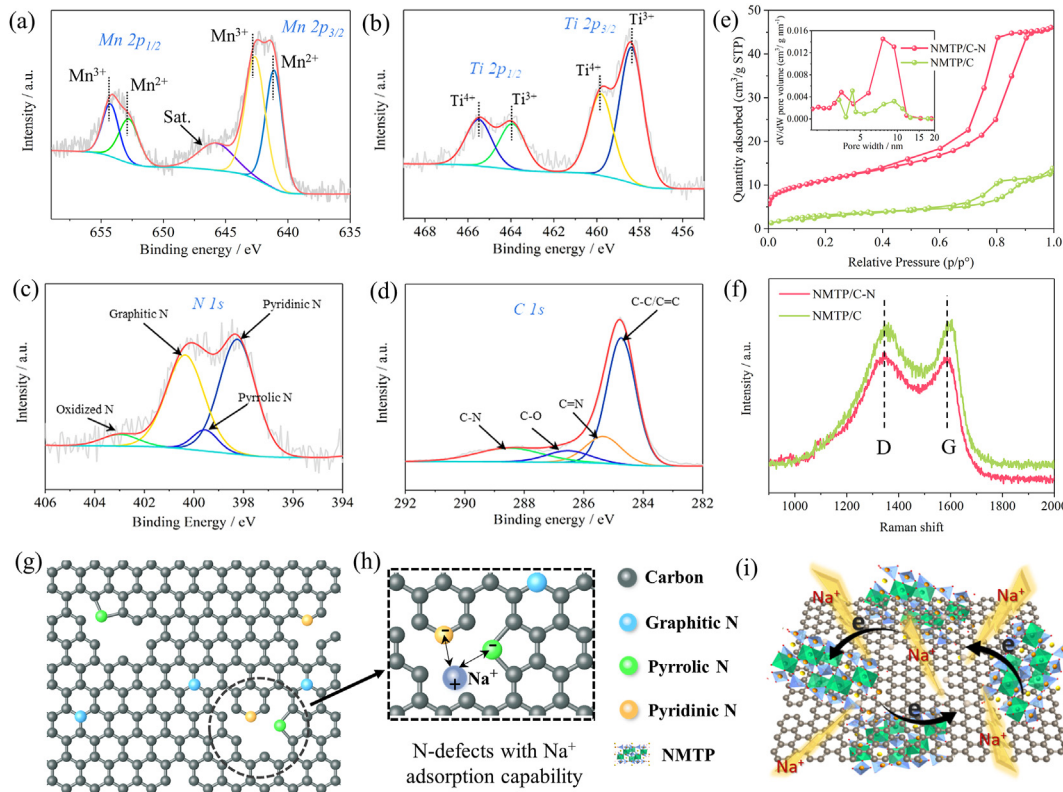


Fig. 2. (a) The high-resolution XPS spectra of Mn 2p, (b) Ti 2p, (c) N 1s, and (d) C 1s in NMTP/C–N. The inset is the pore size distribution curve. (f) Raman spectra of the two samples. (g) The schematic illustration of the structure of N-doped carbon and (h) interaction between N-defects and Na^+ . (i) Schematic illustration of the NMTP/C–N with fast ion/electronic exchange and sodium storage behavior.

was enlarged as the current density increases. Only 25.6 mAh/g of specific capacity was maintained at 5C. The inferior rate performance has probably resulted from the low electronic conductivity of the pure carbon matrix [35]. The long cycling capability of the

electrodes was evaluated at 2C. The NMTP/C–N exhibits a discharge capacity of 54.4 mAh/g in the first cycle. After 350 cycles, a reversible capacity of 47.9 mAh/g can be maintained, which corresponds to 88.1% of capacity retention (Fig. 3c). Charge/discharge

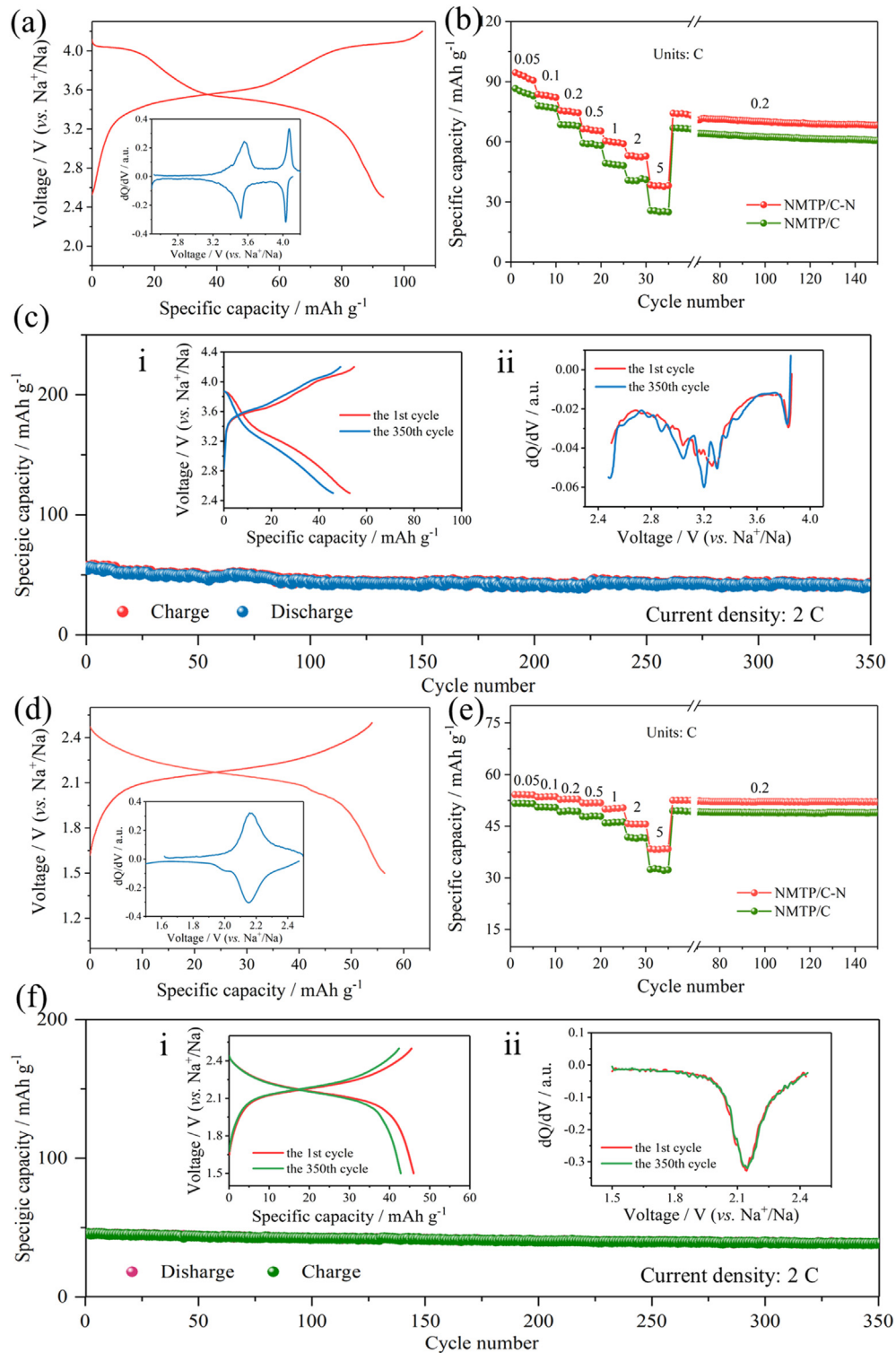


Fig. 3. Electrochemical performances of the NMTP-C and NMTP/C–N materials as both the cathode and anode. (a) Galvanostatic charge/discharge curves of NMTP/C–N in the first cycle at 0.05C as a cathode and their dQ/dV plots. (b) Rate performance and cycling stability of the cathodes at different C-rate. (c) Capacity of the cathode during 350 cycles at 2C and the insets are charge/discharge profiles (i) and the dQ/dV plots (ii) of the 1st and 350th cycle. (d) Galvanostatic charge/discharge curves of NMTP/C–N in the first cycle at 0.05C as an anode and their dQ/dV plots. (e) Rate performance and cycling stability of the anodes at different C-rate. (f) Capacity of the anode during 350 cycles at 2C and the insets are charge/discharge profiles (i) and the dQ/dV plots (ii) of the 1st and 500th cycle.

curves of the cathode in the first and 350th cycle coupled with their discharge dQ/dV plots were plotted in the inset. The dQ/dV patterns show that the main redox peaks shift left slightly, indicating a reduced working potential of the material after 350 cycles, which can also be seen from its discharge curves.

As an anode for $\text{Na}_3\text{MnTi}(\text{PO}_4)_3$, only one sodium-ion per formula can participate in the insertion/extraction reaction, contributing a theoretical capacity of 58.7 mAh/g. To match the cathode, here, a current density of 1C was set as 100 mA/g. As shown in Fig. 3d, the NMTP/C–N delivers a charge capacity of 54.0 mAh/g at 0.05C. In addition, the initial Coulombic efficiency (ICE) is approaching 96.4%. Such high ICE is vitally important in full cell systems [36,37]. Its charge/discharge profiles demonstrate only one voltage plateau at 2.16/2.15 V, which is based on the redox of $\text{Ti}^{3+}/\text{Ti}^{4+}$. The rate capability of the materials was also investigated. As shown in Fig. 3e, the NMTP/C–N anodes exhibit excellent rate capability, with a charge capacity of 54.2, 53.4, 52.7, 51.8, 49.9, and 45.7 mAh/g at 0.05, 0.1, 0.2, 0.5, 1, and 2C, respectively. Even at the high current density of 5C, its charge capacity remains 38.4 mAh/g. When the current density turns back to 0.2C, the specific capacity of the electrode recovers to 52.5 mAh/g and maintains 99% of its initial charge capacity after 100 cycles, demonstrating outstanding rate performance and structural stability. In the case of NMTP/C, despite good cycling stability at 0.2C, its charge capacity is lower than NMTP/C–N at various C-rates. The NMTP/C–N anode also demonstrates superior long cycling stability. As shown in Fig. 3f, the anode exhibits a charge capacity of 45.5 mAh/g in the first cycle at 2C. After 350 cycles, there is still 93.2% of its initial charge capacity remained. The charge/discharge curves (inset i in Fig. 3f) present unchangeable working potentials of the electrode, which is further confirmed by the dQ/dV plots (inset ii in Fig. 3f). The N-doped carbon matrix is key to such good performance. Firstly, the N-doped carbon matrix has higher electronic conductivity, leading to better rate capability. Besides, the carbon material can protect the NMTP from contacting with electrolytes to avoid side reactions. Furthermore, it helps to mitigate the stress caused by the volume change of the NMTP during the repeated sodium-ion intercalation/deintercalation, and thus inhibiting structural degradation of the electrode [38,39].

Generally, sodium storage mechanism includes the non-Faradic double layer effect, Faradaic diffusion-controlled sodium-ion insertion/extraction reactions, and redox-reaction-based [40,41]. In the case of NMTP/C–N, the contribution of pseudocapacitance should be considered because the N-doped carbon can offer more active sites and defects on the surface of the materials for sodium storage. To understand the sodium storage mechanism, the pseudocapacitance contribution of the NMTP/C–N and NMTP/C was calculated based on their cyclic voltammetry (CV) plots at different scan rates from 0.1 to 0.5 mV/s (Fig. 4a–f). The cathodes exhibit four peaks noted as M1, M1', M2, and M2' during the cathodic and anodic processes, whereas the anodes appear two peaks marked as T1 and T1'. The calculation was according to the following Equations (1) and (2) [42,43]:

$$i = a v^b \quad (1)$$

$$\log i = b \times \log v + \log a w \quad (2)$$

here i represents current density, v stands for scan rate, and both a and b are adjustable parameters. For a typical diffusion-controlled reaction, the value of b is 0.5, whereas for an ideal capacitive process, b is 1 [44]. As shown in Fig. 4c and f, b -values for M1, M1', M2, M2', T1, and T1' are 0.69, 0.65, 0.81, 0.53, 0.74, and 0.77, respectively. All b -values are >0.5 , indicating the pseudocapacitance behavior in NMTP/C–N, and since the b -values for the anode are

mostly larger than the cathode, the anode is supposed to possess a larger degree of pseudocapacitance. As shown in Fig. 4g and h, the pseudocapacitance increases as the scan rate increase. The contribution of pseudocapacitance was calculated to be 51.4% under the scan rate of 0.5 mV/s for the cathode (Fig. 4c) and 68.3% for the anode (Fig. 4f). Therefore, it can be deduced that the satisfactory high-rate performance of the NMTP/C–N should attribute to the pseudocapacitance. As the NMTP/C–N shows higher pseudocapacitance contribution than that of the NMTP/C, the N-doped carbon matrix with abundant defects and porous structure is key to the enhanced pseudocapacitance.

Although the enhanced pseudocapacitance in carbon-modified composite materials has been discovered in several previous literature, few explained the mechanism, which is very important for material design. To better understand the role of N-defects in carbon materials toward the enhanced pseudocapacitance and reaction kinetics, the density functional theory (DFT) calculations were used. The adsorption energies of Na on various N-defect sites, which are determined by XPS spectra of N 1s (Fig. 2c), were studied. As shown in Fig. 5a–d, the Na adsorption energies on graphitic-N, pyridinic-N, and pyrrolic-N are -3.014 , -3.180 , and -3.503 eV, respectively, which are much smaller than that of the graphitic-C (-1.191 eV). Therefore, it can be deduced that the N-defects can facilitate Na adsorption on the surface of the carbon matrix. To trigger a redox reaction, Na should pass through the carbon matrix and react with the NMTP active materials. The energy barriers of Na passing through carbon should be as low as possible to ensure fast sodium diffusion and redox reactions. The models of Na passing through various N-vacancy (NV) defects are studied. For comparison, similar carbon defects (CV) are also studied. As depicted in Figs. 5f,g and S4, it shows that compared to the high energy barrier of 20.692 eV for graphitic-C, the introduction of pyridinic-NV and pyrrolic-NV defects significantly reduce the energy barriers to 7.296 and 3.467 eV, respectively. Besides, the energy barriers for Na passing through pyridinic-CV and pyrrolic-CV defects are higher. Therefore, the existence of an N atom is important for facile sodium diffusion. Lower energy barriers for sodium diffusion greatly facilitate the sodium storage process. The apparent diffusion coefficients ($D_{\text{Na}+}$) were calculated based on Fig. S5, and the calculation results are listed in Tables S1 and S2 (for calculation details please see Supplementary Material). It shows that the NMTP/C–N demonstrates a larger $D_{\text{Na}+}$ than the NMTP/C sample. The $D_{\text{Na}+}$ varies between 2.38×10^{-11} and 9.49×10^{-10} for NMTP/C–N, which is comparable and even better than some other carbon-modified NASICON-structured materials [45–48]. The greatly improved charge-transfer and sodium-diffusion kinetics in NMTP/C–N were also verified by the electrochemical impedance spectroscopy, as demonstrated in Fig. S6. So, the stronger adsorption and low energy barriers of N-defects synergistically enhanced the pseudocapacitance and reaction kinetics of the materials for sodium storage.

It is worth noting that, the contribution of pseudocapacitance is important for the high-rate capability and long cycling capacity retention of electrode materials. With the enhanced pseudocapacitance effect and reaction kinetics, NMTP/C–N is capable to be used as a promising bifunctional electrode material for symmetric batteries. A non-aqueous symmetric full cell using this NMTP/C–N material as both the cathode and anode was assembled to show its feasibility for practical utilizations (Fig. 6a,b). An organic solution of 1 M NaClO_4 in PC with 5% FEC was used as the electrolyte. According to the charge/discharge curves in Fig. 6c, the NMTP/C–N full cell can deliver charge and discharge capacities of 108.0 and 91.8 mAh/g, respectively, at 0.05C, with a high ICE of reaching 85.0%. The capacities were calculated based on the cathode. The corresponding dQ/dV plots demonstrate two pairs of symmetric

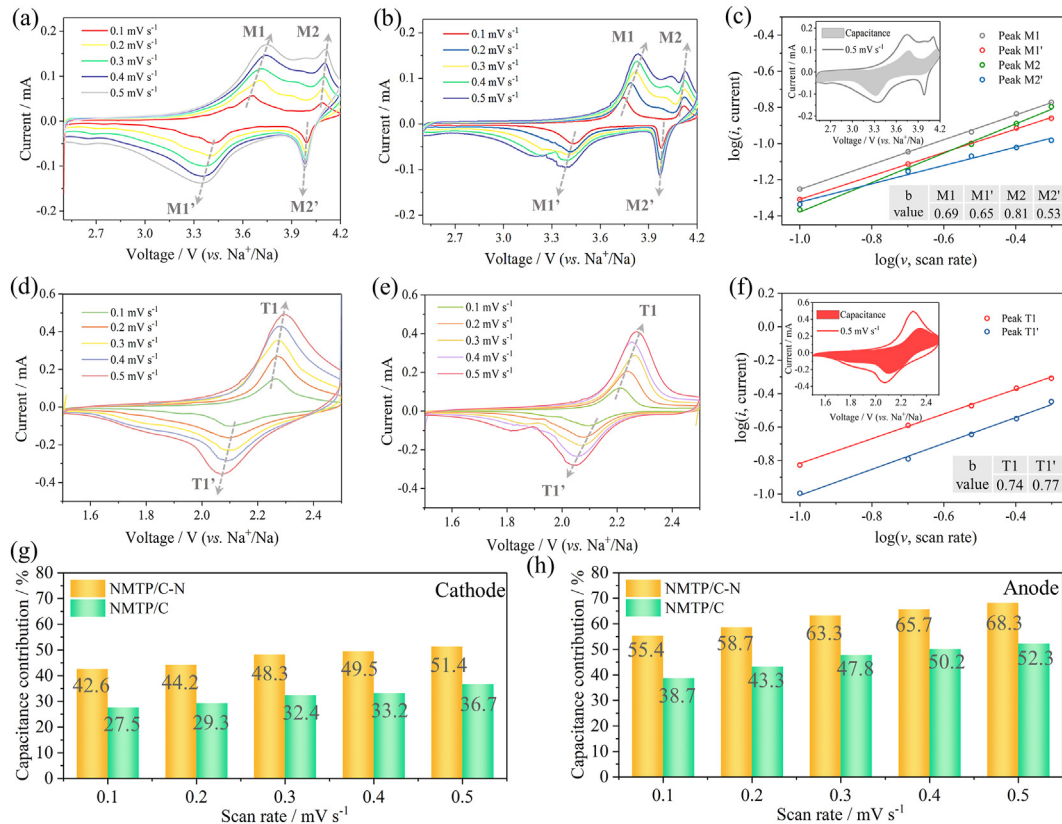


Fig. 4. Kinetics and the Na^+ storage mechanism analysis. (a) CV plots of the NMTP/C–N and (b) NMTP/C at different scan rates within the voltage range of 2.5–4.2 V. (c) The $\log(i)$ vs. $\log(v)$ plots of NMTP/C–N at different charge states. The inset shows the calculated pseudocapacitance (grey) of NMTP/C–N cathode based on the CV curve at the scan rate of 0.5 mV/s. (d) CV plots of the NMTP/C–N and (e) NMTP/C at different scan rates within the voltage range of 1.5–2.5 V. (f) The $\log(i)$ vs. $\log(v)$ plots of NMTP/C–N at different charge states. The inset shows the calculated pseudocapacitance (red) of NMTP/C–N anode based on the CV curve at the scan rate of 0.5 mV/s. (g) Capacitance contribution of NMTP/C–N and NMTP/C at different scan rates as the cathode and (h) anode materials, respectively.

redox potentials at 1.42/1.34 and 1.92/1.88 V, which are derived from the voltage difference between $\text{Mn}^{2+}/\text{Mn}^{3+}$, $\text{Mn}^{3+}/\text{Mn}^{4+}$, and $\text{Ti}^{4+}/\text{Ti}^{3+}$, respectively. Working voltage (the average working

voltage is 1.35 V) and specific capacity of the full cell are higher than its aqueous counterpart, enabling higher energy density of this system (123 Wh/kg). Rate performance of the full cell was

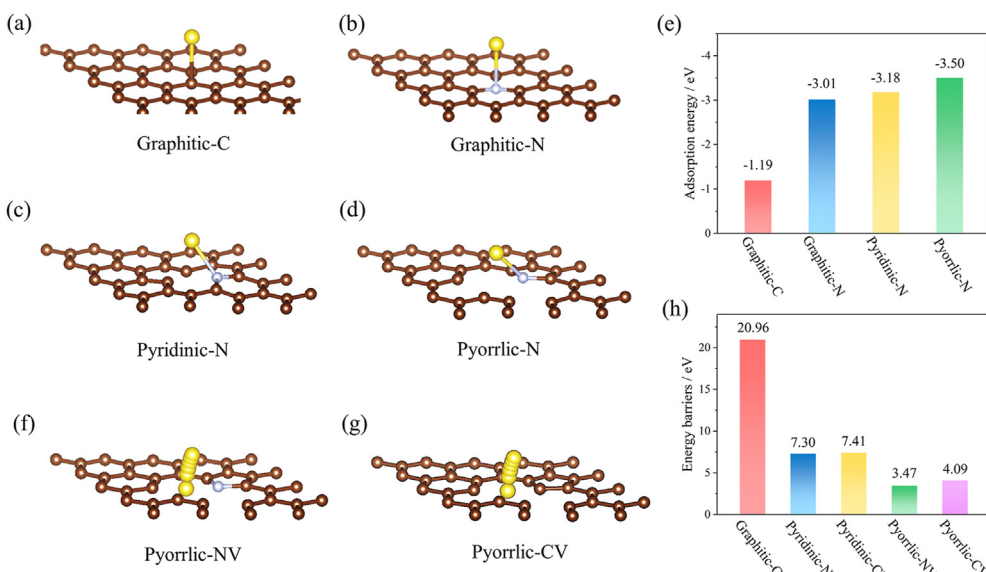


Fig. 5. DFT calculations of Na adsorption and diffusion energies in the carbon matrix. The atomic bonding structures between Na and (a) graphitic-C, (b) graphitic-N, (c) pyridinic-N, (d) pyrrolic-N, and (e) their corresponding adsorption energies with Na. (f) The model of Na passing through pyrrolic-NV defects and (g) pyrrolic-CV defects. (h) Energy barriers of Na passing through various defect structures. In these atomic structures, the brown, grey, and yellow balls represent C, N, and Na atoms, respectively.

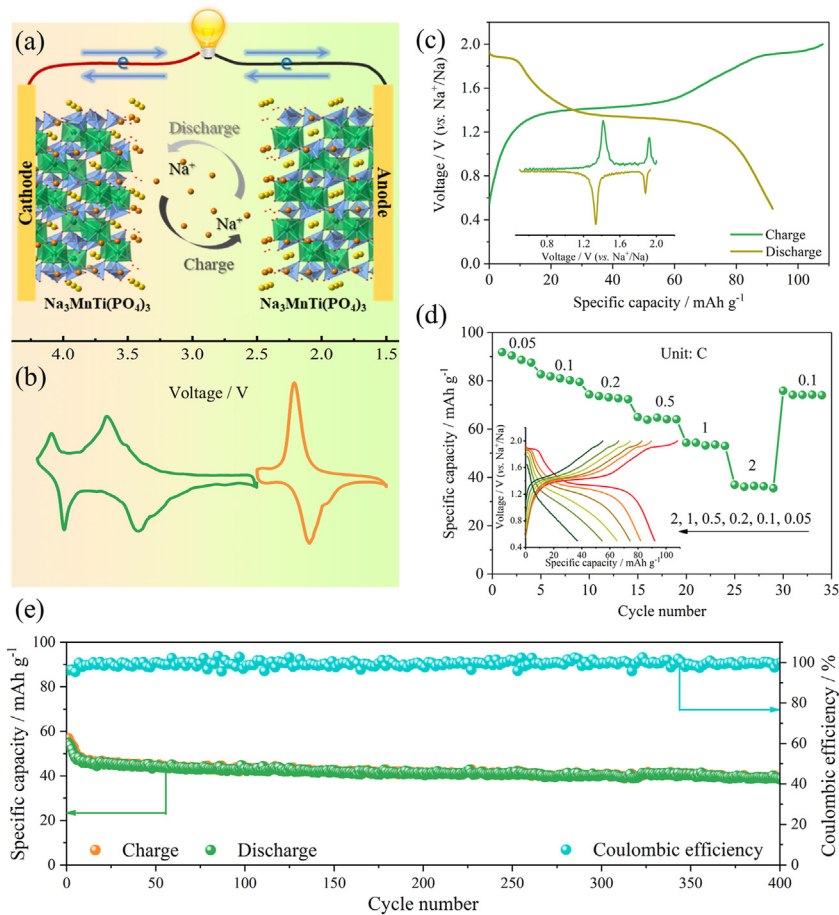


Fig. 6. Electrochemical performance of the symmetric full cell system. (a) Schematic illustration of the construction of the symmetric full cell using NMTP/C–N electrodes. (b) CV curves of NMTP/C–N as the cathode (green) and anode (orange) at the scan rate of 0.1 mV/s. (c) Galvanostatic charge/discharge curves and inset of dQ/dV plots of the initial cycle. (d) Rate performance of the full cell from 0.05 to 2C and inset of the corresponding charge/discharge curves at different rates. (e) Cycling stability of the full cell at 1C.

presented in Fig. 6d, where the NMTP/C–N full cell exhibited discharge capacities of 91.5, 82.7, 74.3, 64.9, 54.3, and 36.9 mAh/g at current densities of 0.05, 0.1, 0.2, 0.5, 1, and 2C, respectively. The energy and power densities of the NMTP/C–N full cell are illustrated in Fig. S7. Note that the NMTP/C–N presents outstanding cycling stability. After 400 cycles at 1C, it can retain a reversible capacity of 40.3 mAh/g, corresponding to 70.9% of its initial capacity (Fig. 6e). The satisfactory sodium storage capability may owe itself to characters of the symmetric systems, which can mitigate volume changes during the repeated sodium exchange. In addition, the N-doped carbon matrix with enhanced electronic conductivity, pseudocapacitance, and the NASICON-structured material with fast ion conductivity are also significantly important.

3. Conclusion

In summary, by embedding $\text{Na}_3\text{MnTi}(\text{PO}_4)_3$ particulates in the N-doped carbon matrix, reaction kinetics and pseudocapacitance of $\text{Na}_3\text{MnTi}(\text{PO}_4)_3$ are effectively improved, and thus the NMTP/C–N material achieves a higher capacity and better rate performance. When assembled as a symmetric full cell, the NMTP/C–N full cell demonstrates a reversible capacity of 91.8 mAh/g and a good cycling stability of 70.9% of capacity retention after 400 cycles at 1C. It is found that the introduction of N species not only increases electronic conductivity, but also causes abundant active sites and

defects structure, which is beneficial to adsorb sodium-ions and reducing the energy barrier for sodium-ion passing through the carbon layer for a redox reaction, enabling enhanced pseudocapacitance effect. This work not only provided a promising bifunctional electrode material, but also deepens our understanding of materials design for enhanced pseudocapacitance and electrochemical performances.

Credit author statement

Huangxu Li: Methodology, Investigation, Data analysis, Writing—Original Draft; **Wei Zhang:** Methodology, Investigation; **Zexun Han:** DFT calculation; **Kena Sun:** DFT calculation; **Chunhui Gao:** Data analysis, Revision; **Ke Cheng:** Data analysis, Revision; **Zhiyang Liu:** Data analysis, Revision; **Qingxin Chen:** Data analysis, Revision; **Jie Zhang:** Data analysis, Revision; **Yanqing Lai:** Resources, Funding acquisition; **Zhian Zhang*:** Resources, Funding acquisition, Supervision, Editing, Project administration; **Hongyan Sun*:** Resources, Supervision, Editing, Project administration.

Declaration of Competing Interest

The authors declare that they have no known competing financial interests or personal relationships that could have appeared to influence the work reported in this paper.

Acknowledgments

This work is supported by the Fundamental Research Funds for the Central Universities of Central South University (Grant No. 2020zzts467, 2020zzts475, and CX20200180).

Appendix A. Supplementary data

Supplementary data to this article can be found online at <https://doi.org/10.1016/j.mtener.2021.100754>.

References

- [1] S. Chu, Y. Cui, N. Liu, The path towards sustainable energy, *Nat. Mater.* 16 (2016) 16–22.
- [2] D. Larcher, J.M. Tarascon, Towards greener and more sustainable batteries for electrical energy storage, *Nat. Chem.* 7 (2015) 19–29.
- [3] N. Kittner, F. Lill, D.M. Kammen, Energy storage deployment and innovation for the clean energy transition, *Nature Energy* 2 (2017) 17125.
- [4] H. Li, X. Zhou, W. Zhai, S. Lu, J. Liang, Z. He, H. Long, T. Xiong, H. Sun, Q. He, Z. Fan, H. Zhang, Phase engineering of nanomaterials for clean energy and catalytic applications, *Adv. Energy Mater.* 10 (2020) 2002019.
- [5] B. Scrosati, J. Hassoun, Y.-K. Sun, Lithium-ion batteries. A look into the future, *Energy Environ. Sci.* 4 (2011) 3287–3295.
- [6] C. Gao, Q. Dong, G. Zhang, H. Fan, H. Li, B. Hong, Y. Lai, Antimony-doped lithium phosphate artificial solid electrolyte interphase for dendrite-free lithium-metal batteries, *ChemElectroChem* 6 (2019) 1134–1138.
- [7] Y. Huang, H. Yang, T. Xiong, D. Adekoya, W. Qiu, Z. Wang, S. Zhang, M.S. Bologun, Adsorption energy engineering of nickel oxide hybrid nanosheets for high areal capacity flexible lithium-ion batteries, *Energy Storage Mater.* 25 (2020) 41–51.
- [8] M.S. Bologun, Y. Zeng, W. Qiu, Y. Luo, A. Onasanya, T.K. Olaniyi, Y. Tong, Three-dimensional nickel nitride (Ni_3N) nanosheets: free standing and flexible electrodes for lithium ion batteries and supercapacitors, *J. Mater. Chem. A* 4 (2016) 9844–9849.
- [9] M.S. Bologun, Z. Wu, Y. Luo, W. Qiu, X. Fan, B. Long, M. Huang, P. Liu, Y. Tong, High power density nitridated hematite ($\alpha\text{-Fe}_2\text{O}_3$) nanorods as anode for high-performance flexible lithium ion batteries, *J. Power Sources* 308 (2016) 7–17.
- [10] C. Delmas, Sodium and sodium-ion batteries: 50 Years of research, *Adv. Energy Mater.* 8 (2018) 1703137.
- [11] T. Jin, H. Li, K. Zhu, P.-F. Wang, P. Liu, L. Jiao, Polyanion-type cathode materials for sodium-ion batteries, *Chem. Soc. Rev.* 49 (2020) 2342–2377.
- [12] W. Zhang, Z. Zhang, H. Li, D. Wang, T. Wang, X. Sun, J. Zheng, Y. Lai, Engineering 3D well-interconnected $\text{Na}_4\text{MnV}(\text{PO}_4)_3$ facilitates ultrafast and ultrastable sodium storage, *ACS Appl. Mater. Interfaces* 11 (2019) 35746–35754.
- [13] Y. Noguchi, E. Kobayashi, L.S. Plashnitsa, S. Okada, J.-i. Yamaki, Fabrication and performances of all solid-state symmetric sodium battery based on NASICON-related compounds, *Electrochim. Acta* 101 (2013) 59–65.
- [14] L. Zhang, B. Zhang, C. Wang, Y. Dou, Q. Zhang, Y. Liu, H. Gao, M. Al-Mamun, W.K. Pang, Z. Guo, S.X. Dou, H.K. Liu, Constructing the best symmetric full K-ion battery with the NASICON-type $\text{K}_3\text{V}_2(\text{PO}_4)_3$, *Nanomater. Energy* 60 (2019) 432–439.
- [15] X. Yao, Z. Zhu, Q. Li, X. Wang, X. Xu, J. Meng, W. Ren, X. Zhang, Y. Huang, L. Mai, 3.0 V high energy density symmetric sodium-ion battery: $\text{Na}_4\text{V}_2(\text{PO}_4)_3$ parallel $\text{Na}_3\text{V}_2(\text{PO}_4)_3$, *ACS Appl. Mater. Interfaces* 10 (2018) 10022–10028.
- [16] C. Wang, L. Zhang, M. Al-Mamun, Y. Dou, P. Liu, D. Su, G. Wang, S. Zhang, D. Wang, H. Zhao, A hollow-shell structured V_2O_5 electrode-based symmetric full Li-ion battery with highest capacity, *Adv. Energy Mater.* 9 (2019) 1900909.
- [17] Y. Wang, R. Xiao, Y.S. Hu, M. Avdeev, L. Chen, $\text{P}_2\text{-Na}_{0.6}\text{[Cr}_{0.5}\text{Ti}_{0.4}\text{]O}_2$ cation-disordered electrode for high-rate symmetric rechargeable sodium-ion batteries, *Nat. Commun.* 6 (2015) 6954.
- [18] S. Guo, H. Yu, P. Liu, Y. Ren, T. Zhang, M. Chen, M. Ishida, H. Zhou, High-performance symmetric sodium-ion batteries using a new bipolar O3-type material, $\text{Na}_{0.8}\text{Ni}_{0.4}\text{Ti}_{0.6}\text{O}_2$, *Energy Environ. Sci.* 8 (2015) 1237–1244.
- [19] H. Li, T. Jin, X. Chen, Y. Lai, Z. Zhang, W. Bao, L. Jiao, Rational architecture design enables superior Na storage in greener NASICON- $\text{Na}_4\text{MnV}(\text{PO}_4)_3$ cathode, *Adv. Energy Mater.* 8 (2018) 1801418.
- [20] W. Zhang, H. Li, Z. Zhang, M. Xu, Y. Lai, S.L. Chou, Full activation of $\text{Mn}(+4)/\text{Mn}(3+)$ redox in $\text{Na}_4\text{MnCr}(\text{PO}_4)_3$ as a high-voltage and high-rate cathode material for sodium-ion batteries, *Small* 16 (2020), e2001524.
- [21] X. Liu, X. Jiang, F. Zhong, X. Feng, W. Chen, X. Ai, H. Yang, Y. Cao, High-safety symmetric sodium-ion batteries based on nonflammable phosphate electrolyte and double $\text{Na}_3\text{V}_2(\text{PO}_4)_3$ electrode, *ACS Appl. Mater. Interfaces* 11 (2019) 27833–27838.
- [22] D. Wang, X. Bie, Q. Fu, D. Dixon, N. Bramnik, Y.S. Hu, F. Fauth, Y. Wei, H. Ehrenberg, G. Chen, F. Du, Sodium vanadium titanium phosphate electrode for symmetric sodium-ion batteries with high power and long lifespan, *Nat. Commun.* 8 (2017) 15888.
- [23] M. Li, Z. Zuo, J. Deng, Q. Yao, Z. Wang, H. Zhou, W.-B. Luo, H.-K. Liu, S.-X. Dou, A high rate capability and long lifespan symmetric sodium-ion battery system based on a bipolar material $\text{Na}_2\text{V}_2(\text{PO}_4)_3/\text{C}$, *J. Mater. Chem. A* 6 (2018) 9962–9970.
- [24] H. Gao, J.B. Goodenough, An aqueous symmetric sodium-ion battery with NASICON-structured $\text{Na}_3\text{MnTi}(\text{PO}_4)_3$, *Angew. Chem.* 128 (2016) 12960–12964.
- [25] H. Gao, Y. Li, K. Park, J.B. Goodenough, Sodium extraction from NASICON-structured $\text{Na}_3\text{MnTi}(\text{PO}_4)_3$ through $\text{Mn}(\text{III})/\text{Mn}(\text{II})$ and $\text{Mn}(\text{IV})/\text{Mn}(\text{III})$ redox couples, *Chem. Mater.* 28 (2016) 6553–6559.
- [26] M. Chen, L. Chen, Z. Hu, Q. Liu, B. Zhang, Y. Hu, Q. Gu, J.L. Wang, L.Z. Wang, X. Guo, S.L. Chou, S.X. Dou, Carbon-coated $\text{Na}_{3.32}\text{Fe}_{2.34}(\text{P}_2\text{O}_7)_2$ cathode material for high-rate and long-life sodium-ion batteries, *Adv. Mater.* 29 (2017) 1605535.
- [27] D. Xu, D. Chao, H. Wang, Y. Gong, R. Wang, B. He, X. Hu, H. Fan, Flexible quasi-solid-state sodium-ion capacitors developed using 2D metal–organic-framework array as reactor, *Adv. Energy Mater.* 8 (2018) 1702769.
- [28] H. Li, X. Chen, T. Jin, W. Bao, Z. Zhang, L. Jiao, Robust graphene layer modified $\text{Na}_2\text{MnP}_2\text{O}_7$ as a durable high-rate and high energy cathode for Na-ion batteries, *Energy Storage Mater.* 16 (2019) 383–390.
- [29] H. Li, Z. Zhang, M. Xu, W. Bao, Y. Lai, K. Zhang, J. Li, Triclinic off-stoichiometric $\text{Na}_{3.12}\text{Mn}_{2.44}(\text{P}_2\text{O}_7)_2/\text{C}$ cathode materials for high-energy/power sodium-ion batteries, *ACS Appl. Mater. Interfaces* 10 (2018) 24564–24572.
- [30] H. Li, M. Xu, C. Gao, W. Zhang, Z. Zhang, Y. Lai, L. Jiao, Highly efficient, fast and reversible multi-electron reaction of $\text{Na}_3\text{MnTi}(\text{PO}_4)_3$ cathode for sodium-ion batteries, *Energy Storage Mater.* 26 (2020) 325–333.
- [31] T. Zhu, P. Hu, X. Wang, Z. Liu, W. Luo, K.A. Owusu, W. Cao, C. Shi, J. Li, L. Zhou, L. Mai, Realizing three-electron redox reactions in NASICON-structured $\text{Na}_3\text{MnTi}(\text{PO}_4)_3$ for sodium-ion batteries, *Adv. Energy Mater.* 9 (2019) 1803436.
- [32] W. Shen, H. Li, Z. Guo, C. Wang, Z. Li, Q. Xu, H. Liu, Y. Wang, Y. Xia, Double-nanocarbon synergistically modified $\text{Na}_3\text{V}_2(\text{PO}_4)_3$: an advanced cathode for high-rate and long-life sodium-ion batteries, *ACS Appl. Mater. Interfaces* 8 (2016) 15341–15351.
- [33] Y. Jiang, X. Zhou, D. Li, X. Cheng, F. Liu, Y. Yu, Highly reversible Na storage in $\text{Na}_3\text{V}_2(\text{PO}_4)_3$ by optimizing nanostructure and rational surface engineering, *Adv. Energy Mater.* 8 (2018) 1800068.
- [34] M. Xu, T. Li, L. Fei, H. Li, X. Guo, P. Hou, Y. Ying, W. Zhu, Y. Zhou, Y. Lin, Z. Zhang, Y. Lai, Y. Zhu, H. Zhang, H. Huang, Thermodynamically metal atom trapping in van der Waals layers enabling multifunctional 3D carbon network, *Adv. Funct. Mater.* 30 (2020) 2002626.
- [35] Y. Yao, Y. Jiang, H. Yang, X. Sun, Y. Yu, $\text{Na}_3\text{V}_2(\text{PO}_4)_3$ coated by N-doped carbon from ionic liquid as cathode materials for high rate and long-life Na-ion batteries, *Nanoscale* 9 (2017) 10880–10885.
- [36] H. Li, L. Peng, Y. Zhu, D. Chen, X. Zhang, G. Yu, An advanced high-energy sodium ion full battery based on nanostructured $\text{Na}_2\text{Ti}_3\text{O}_7/\text{VOPO}_4$ layered materials, *Energy Environ. Sci.* 9 (2016) 3399–3405.
- [37] M. Chen, L. Chen, Z. Hu, Q. Liu, B. Zhang, Y. Hu, Q. Gu, J.-L. Wang, L.-Z. Wang, X. Guo, S.-L. Chou, S.-X. Dou, Carbon-coated $\text{Na}_{3.32}\text{Fe}_{2.34}(\text{P}_2\text{O}_7)_2$ cathode material for high-rate and long-life sodium-ion batteries, *Adv. Mater.* 29 (2017) 1605535.
- [38] X. Rui, W. Sun, C. Wu, Y. Yu, Q. Yan, An advanced sodium-ion battery composed of carbon coated $\text{Na}(3)\text{V}(2)(\text{PO}_4)(3)$ in a porous graphene network, *Adv. Mater.* 27 (2015) 6670–6676.
- [39] T. Wang, W. Zhang, H. Li, J. Hu, Y. Lai, Z. Zhang, N-doped carbon nanotubes decorated $\text{Na}_3\text{V}_2(\text{PO}_4)_2\text{F}_3$ as a durable ultrahigh-rate cathode for sodium ion batteries, *ACS Appl. Energy Mater.* 3 (2020) 3845–3853.
- [40] V. Augustyn, J. Come, M.A. Lowe, J.W. Kim, P.L. Taberna, S.H. Tolbert, H.D. Abruna, P. Simon, B. Dunn, High-rate electrochemical energy storage through Li^+ intercalation pseudocapacitance, *Nat. Mater.* 12 (2013) 518–522.
- [41] C. Chen, Y. Wen, X. Hu, X. Ji, M. Yan, L. Mai, P. Hu, B. Shan, Y. Huang, $\text{Na}(+)$ intercalation pseudocapacitance in graphene-coupled titanium oxide enabling ultra-fast sodium storage and long-term cycling, *Nat. Commun.* 6 (2015) 6929.
- [42] Q. Wei, Y. Jiang, X. Qian, L. Zhang, Q. Li, S. Tan, K. Zhao, W. Yang, Q. An, J. Guo, L. Mai, Sodium ion capacitor using pseudocapacitive layered ferric vanadate nanosheets cathode, *iScience* 6 (2018) 212–221.
- [43] D. Chao, C. Zhu, P. Yang, X. Xia, J. Liu, J. Wang, X. Fan, S.V. Savilov, J. Lin, H.J. Fan, Z.X. Shen, Array of nanosheets render ultrafast and high-capacity Na-ion storage by tunable pseudocapacitance, *Nat. Commun.* 7 (2016) 12122.
- [44] Z. Le, F. Liu, P. Nie, X. Li, X. Liu, Z. Bian, G. Chen, H.B. Wu, Y. Lu, Pseudocapacitive sodium storage in mesoporous single-crystal-like TiO_2 -graphene nanocomposite enables high-performance sodium-ion capacitors, *ACS Nano* 11 (2017) 2952–2960.
- [45] D. Wang, X. Bie, Q. Fu, D. Dixon, N. Bramnik, Y. Hu, F. Fauth, Y. Wei, H. Ehrenberg, G. Chen, F. Du, Sodium vanadium titanium phosphate electrode for symmetric sodium-ion batteries with high power and long lifespan, *Nat. Commun.* 8 (2017) 15888.
- [46] Q. Zhu, X. Chang, N. Sun, H. Liu, R. Chen, F. Wu, B. Xu, Microorganism moulded pomegranate-like $\text{Na}_3\text{V}_2(\text{PO}_4)_3/\text{C}$ nanocomposite for advanced sodium-ion battery, *J. Mater. Chem. A* 5 (2017) 9982–9990.
- [47] D. Zhang, P. Feng, B. Xu, Z. Li, J. Qiao, J. Zhou, C. Chang, High rate performance of $\text{Na}_3\text{V}_2\text{-cu}_x(\text{PO}_4)_3/\text{C}$ cathodes for sodium ion batteries, *J. Electrochem. Soc.* 164 (2017) A3563–A3569.
- [48] J. Liu, K. Tang, K. Song, P. Aken, Y. Yu, J. Maier, Electrospun $\text{Na}_3\text{V}_2(\text{PO}_4)_3/\text{C}$ nanofibers as stable cathode materials for sodium-ion batteries, *Nanoscale* 6 (2014) 5081–5087.